Journal of Nanobiotechnology

RESEARCH Open Access

NEP_{1-40}-modified human serum albumin nanoparticles enhance the therapeutic effect of methylprednisolone against spinal cord injury

Yan Lin[1†], Chunhong Li[1†], Jian Li[1†], Ruolan Deng[1†], Juan Huang[2†], Qinglian Zhang[2], Jiayao Lyu[1], Na Hao[1*] and Zhirong Zhong[1,3,4*]

Abstract

Background: Frequent injection of high-dose methylprednisolone (MP) is used to treat spinal cord injury (SCI), but free MP is associated with various side effects and its water solubility is low, limiting potential dosing regimes and administration routes. Albumin-based nanoparticles, which can encapsulate therapeutic drugs and release cargo in a controlled pattern, show high biocompatibility and low toxicity. The Nogo protein, expressed on the surface of oligodendrocytes, can inhibit axonal growth by binding with the axonal Nogo receptor (NgR). Peptide NEP_{1-40}, an NgR antagonist, can bind specifically to Nogo, significantly improving functional recovery and axon growth in the corticospinal tract. Therefore, we hypothesized that delivering MP within nanoparticles decorated with NEP_{1-40} could avoid the disadvantages of free MP and enhance its therapeutic efficacy against SCI.

Results: We used human serum albumin to prepare MP-loaded NPs (MP-NPs), to whose surface we conjugated NEP_{1-40} to form NEP_{1-40}-MP-NPs. Transmission electron microscopy indicated successful formation of nanoparticles. NEP_{1-40}-MP-NPs were taken up significantly better than MP-NPs by the Nogo-positive cell line RSC-96 and were associated with significantly higher Basso–Beattie–Bresnahan locomotor scores in rats recovering from SCI. Micro-computed tomography assay showed that NEP_{1-40}-MP-NPs mitigated SCI-associated loss of bone mineral density and accelerated spinal cord repair.

Conclusions: NEP_{1-40}-MP-NPs can enhance the therapeutic effects of MP against SCI. This novel platform may also be useful for delivering other types of drugs.

Keywords: NEP_{1-40}, Human serum albumin nanoparticles, Methylprednisolone, Spinal cord injury

Background

Spinal cord injury (SCI) often leads to impairment of motor, sensory, and autonomous functions [1], as well as neuronal loss, axonal degeneration, severe neurological deficits, and life-long movement and sensory dysfunction [2, 3]. Statistics from the US indicate that in 2016, approximately 282,000 people were affected by SCI, caused mainly by traffic accidents or falling from heights [4]. SCI has no effective treatment, reflecting its complex and poorly understood mechanisms [5]. Therefore, effective strategies are urgently needed to treat SCI.

High-dose methylprednisolone (MP) has shown neuroprotective efficacy in multicenter trials for limiting injury in SCI [6–8]. MP acts as an antioxidant and anti-inflammatory agent that can also stabilize lysosomal membranes and suppress edema [9–11]. MP can also inhibit apoptosis in oligodendrocytes [12, 13]. On the other

*Correspondence: haona2010@163.com; zhongzhirong@126.com
†Yan Lin, Chunhong Li, Jian Li, Ruolan Deng and Juan Huang contributed equally to this work
[1] Department of Pharmaceutical Sciences, School of Pharmacy, Southwest Medical University, Luzhou 646000, China
Full list of author information is available at the end of the article

hand, high-dose MP can trigger several side effects [14], such as pneumonia [15], gastric ulcer, leukemia, infection and neuropathy [16]. In addition, frequent intravenous injections affect the patient's quality of life. MP shows poor water solubility, which limits the potential dosing regimes and administration routes that can be used.

It may be possible to bypass the disadvantages of free MP by encapsulating it within nanoparticles (NPs) that target the central nervous system (CNS). Indeed, various nanoparticle formulations have been assessed for SCI therapy [14, 17, 18], and some may seal damaged axonal membranes or activate intrinsic anti-oxidation pathways [19–21]. One promising endogenous nanoparticle is human serum albumin (HSA) [22], which is non-toxic, non-antigenic, biocompatible, and biodegradable, and it can bind drugs [23]. Given the abundance and robustness of HSA-NPs [24], many researchers have been trying to load them with therapeutic drugs. HSA-NPs are phagocytosed mainly by macrophages in the reticuloendothelial system, liver, kidney and bone marrow, allowing them to target organs [25]. The abundant free amino acids on the surface of HSA-NPs can be modified with ligands to increase targeting abilities [26, 27].

A promising candidate for targeting NPs to the CNS is the $NEP_{1\text{-}40}$ peptide, which competes with the ability of Nogo, expressed on the surface of oligodendrocytes, to bind to the Nogo receptor (NgR) on axons [28, 29]. Nogo inhibits myelin-derived axon outgrowth and may hinder axonal regeneration following CNS injury [28]. $NEP_{1\text{-}40}$ blocks Nogo-mediated inhibition of axonal outgrowth in the corticospinal tract, improving functional recovery, making it a potential treatment in SCI [28, 30, 31].

We hypothesized that we could enhance the therapeutic efficacy of MP and reduce its toxic effects by encapsulating it within NPs decorated with $NEP_{1\text{-}40}$. We reasoned that this peptide should result in more specific NP targeting than other ligands [30, 31], and the peptide itself has been shown to promote neuronal regeneration in SCI. As a carrier for preparing MP-loaded NPs, we chose human serum albumin, which may be more biocompatible and less toxic than other carriers.

Table 1 Size distribution and zeta potential of nanoparticles

	Particle size (nm)	Zeta potential (mV)	PDI
Blank NPs	74.87 ± 0.19	21.26 ± 0.73	0.225 ± 0.003
MP-NPs	107.76 ± 1.68*	20.53 ± 1.34	0.251 ± 0.001
$NEP_{1\text{-}40}$-MP-NPs	192.19 ± 4.43#	− 8.04 ± 3.99	0.263 ± 0.002

Results are expressed as mean ± SD from three independent experiments

MP methylprednisolone, *NP* nanoparticle, *PDI* polydispersity index

* $P < 0.0001$ vs. MP-NPs and # $P < 0.0001$ vs. $NEP_{1\text{-}40}$-MP-NPs

Results

Characterization of NPs preparations

Blank NPs, MP-loaded NPs (MP-NPs) and $NEP_{1\text{-}40}$-modified MP-NPs (NEP1-40-MP-NPs) were prepared as described in Methods and then characterized using a wide variety of techniques. Blank NPs showed a size of 74.87 ± 0.19 nm and polydispersity index (PDI) of 0.225 ± 0.003 (Table 1). MP loading significantly increased NP size ($P < 0.001$): MP-NPs showed a size of 107.76 ± 1.68 nm and NEP1-40-MP-NPs, a size of 192.19 ± 4.43 nm. NEP1-40-MP-NPs were significantly larger than MP-NPs ($P < 0.001$). Moreover, all types of NPs showed PDIs < 0.3, suggesting homogeneity. Transmission electron microscopy showed that NPs were spherical, MP-NPs were larger than blank NPs, and both NP preparations showed a uniform size distribution (Fig. 1).

Fourier-transform infrared spectroscopy confirmed the formation of MP-NPs (Fig. 2A) and $NEP_{1\text{-}40}$-MP-NPs (Fig. 2B). A peak due to vibrations of the conjugated C=O bond in MP was detected around 1654 cm^{-1} in the spectra of MP, the physical mixture of MP and PEG, and the physical mixture of MP, NHS-PEG5000-MAL and $NEP_{1\text{-}40}$ (Fig. 2A, B, traces a, d, i). Additional peaks were seen in the region of 3250–3408 cm^{-1} corresponding to the O–H bond in MP (Fig. 2A, trace a) and around 3200 cm^{-1} corresponding to the vibration of the O–H bond in PEG (Fig. 2A, trace b). The MP peak around 1654 cm^{-1} was not found in the spectrum of MP-PEG (Fig. 2A, trace c), which was almost identical to that of PEG (Fig. 2A, trace b). The physical mixture of MP and PEG contained characteristic features of the spectra of PEG and MP on their own (Fig. 2A, trace d), suggesting that MP was encapsulated inside PEG to form MP-PEG.

We did not observe a peak for vibration of the unsaturated bond ($\upsilon_{C\text{-}H}$) at 3000-3100 cm^{-1} in the spectrum of NHS-PEG_{5000}-MAL (Fig. 2B, trace *f*). This may be because the peak was obscured by the υ_{O-H} peak around 3400 cm^{-1}. We observed a peak at 1716 cm^{-1} corresponding to $\upsilon_{C=O}$ of the amino ester in NHS-PEG_{5000}-MAL (Fig. 2B, trace *f*), which was absent from the spectrum of NEPI-40-MP-NPs (Fig. 2B, trace *h*). The MP peak around 1654 cm^{-1} was present in the spectrum of the physical mixture of MP, NHS-PEG5000-MAL and $NEP_{1\text{-}40}$ (Fig. 2B, trace *i*), but it was absent from the spectrum of NEPI-40-MP-NPs (Fig. 2B, trace *h*). These results suggest that MP was successfully wrapped in nanoparticles, and that MP-NPs successfully reacted with NHS-PEG_{5000}-MAL.

Infrared spectroscopy could not be used to analyze $NEP_{1\text{-}40}$ or MP-NPs on their own. Nevertheless, HPLC and laser confocal microscopy studies confirmed that

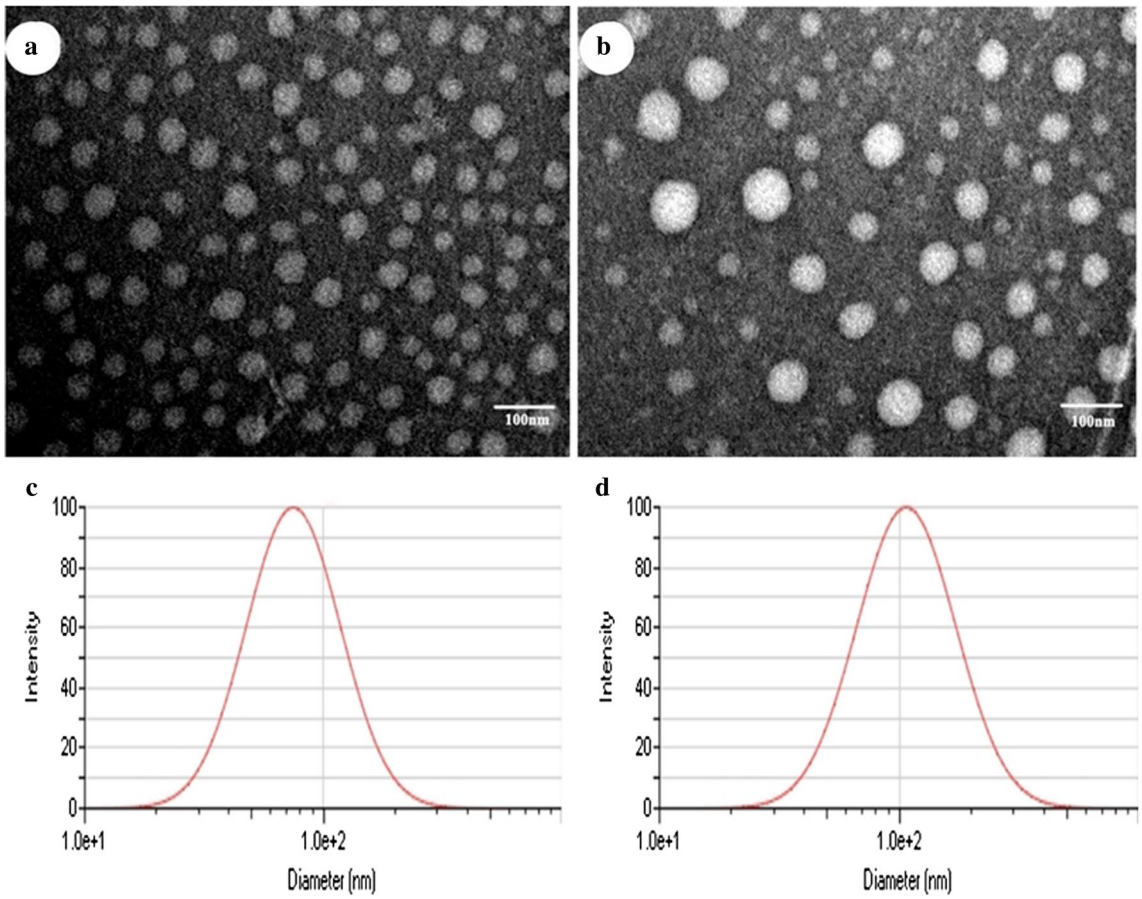

Fig. 1 Morphology of blank NPs (**a**) and MP-NPs (**b**) observed by transmission electron microscopy. Size distribution of blank NPs (**c**) and MP-NPs (**d**) detected by dynamic light scattering

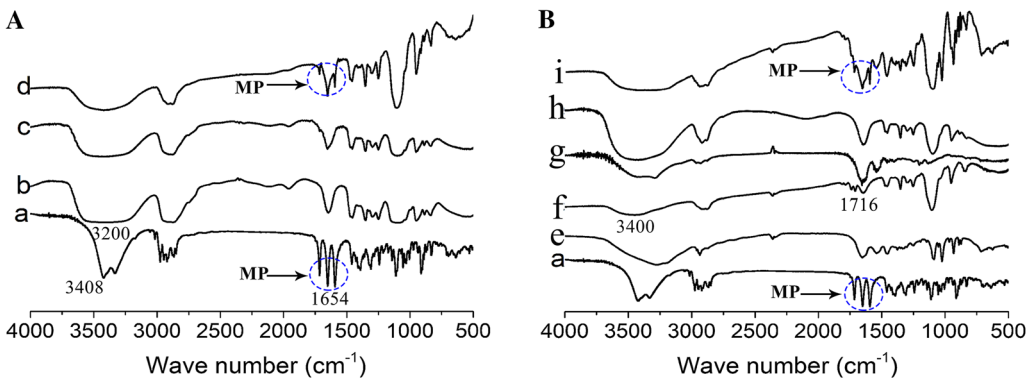

Fig. 2 Fourier-transform infrared spectra of NPs. **A** Spectra of MP (trace *a*), PEG (trace *b*), MP-PEG (trace *c*), and the physical mixture of MP and PEG (trace *d*). Peaks at 3408, 1654 and 3200 cm^{-1} corresponded, respectively, to the free υ_{O-H}, conjugated $\upsilon_{C=O}$ and connective υ_{O-H}. **B** Spectra of MP (trace *a*), blank NPs (trace *e*), NHS-PEG5000-MAL (trace *f*), NEP_{1-40} (trace *g*), NEP1-40-MP-NPs (trace *h*), and the physical mixture of MP, NHS-PEG5000-MAL and NEP_{1-40} (trace *i*). Peaks at 1716 and 3400 cm^{-1} corresponded, respectively, to amino ester $\upsilon_{C=O}$ and connective υ_{O-H}

the NEP_{1-40}-MP-NP delivery system was successfully established. The conjugation of NEP_{1-40} with MP-NPs to form NEP_{1-40}-MP-NPs was confirmed by fluorescently labeling the peptide and then measuring the fluorescence signal of sample retained by the filter and of flow-through that passed through the filter (Additional

file 1: Figure S1). The retained sample was re-filtered a total of five times. Fluorescence intensity (arbitrary units) of the sample decreased from 2938.67 ± 61.85 after the first filtration to 647.47 ± 2.52 after the fifth. The fluorescence intensity of the flow-through was 1397.33 ± 188.54 after the first filtration and became undetectable after the fifth filtration. These results suggest that $NEP_{1\text{-}40}$ was successfully conjugated with MP-NPs to form $NEP_{1\text{-}40}$-MP-NPs. The conjugation rate was calculated to be 70 ± 1.3% (see "Methods").

As a complementary method to fluorescence detection, we quantified the conjugation rate using HPLC. Under our conditions, $NEP_{1\text{-}40}$ eluted as a sharp peak with a retention time of 21 min. In contrast, no such peak was detected in the filtrate from the fifth ultrafiltration. The conjugation rate, 71 ± 0.8%, agreed well with that determined based on fluorescence detection.

Drug encapsulation, loading rate and release in vitro by NPs

MP-NPs showed an encapsulation efficiency of 84.06% ± 3.48% and drug-loading rate of 7.32% ± 0.71%. Cumulative release in vitro during the first 12 h was 59.05 ± 4.08% for $NEP_{1\text{-}40}$-MP-NPs and ~ 85% for free MP (Fig. 3). $NEP_{1\text{-}40}$-MP-NPs showed sustained release without a significant early burst, suggesting that MP was completely encapsulated within nanoparticles rather than being adsorbed on the surface of nanoparticles.

We examined various kinetics models to describe $NEP_{1\text{-}40}$-MP-NPs release in vitro. The models gave the following results: zero-order equation, $Q = 0.4097\ t + 22.3559$ ($R^2 = 0.6551$); first-level equation, $Q = 56.6237\ (1 - e^{-0.0887\ t})$ ($R^2 = 0.9739$); Higuchi equation, $Q = 5.3239\ t^{1/2} + 10.9399$ ($R^2 = 0.8609$); and Ritger–Peppas equation, $Q = 12.7675\ t^{0.3525}$ ($R^2 = 0.9413$). We concluded that the first-level equation best described $NEP_{1\text{-}40}$-MP-NPs release in PBS (pH 7.4) in vitro.

In vitro toxicity detection by hemolysis assay

The hemolytic assay is regarded as a sensitive method to evaluate NPs biosafety. In our study, we sought to evaluate the hemolytic activity of $NEP_{1\text{-}40}$-MP-NPs. In the positive control, ~ 100% hemolysis was observed, compared to only 4.85% for $NEP_{1\text{-}40}$-MP-NPs at concentrations up to 2 mg/mL (Additional file 1: Figure S2). This low level is within the normal range recommended by the ASTM E2524-08 standard. These results demonstrate that $NEP_{1\text{-}40}$-MP-NPs have good

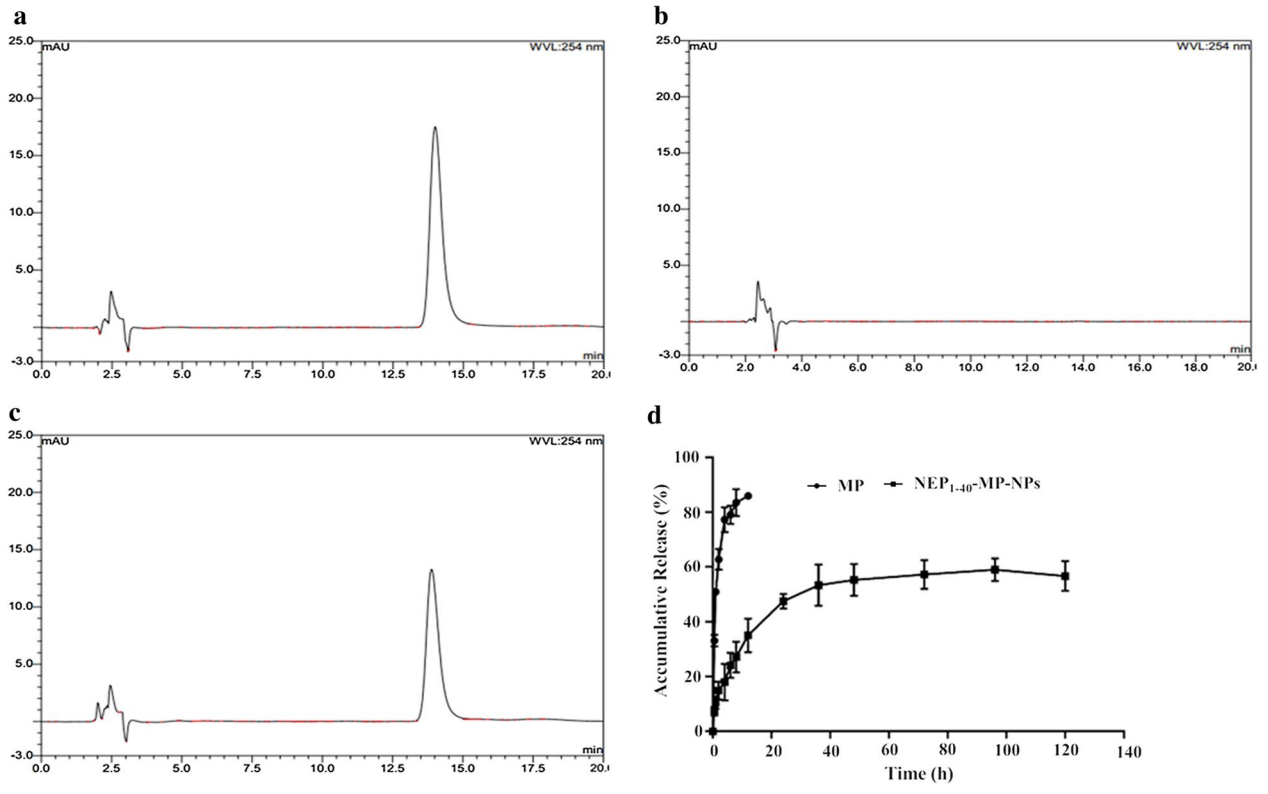

Fig. 3 Cumulative release of MP from $NEP_{1\text{-}40}$-MP-NPs and free MP determined by HPLC. Representative chromatograms of **a** MP, **b** blank NPs, **c** MP-NPs. **d** Quantitation of cumulative release (mean ± SD, n = 3)

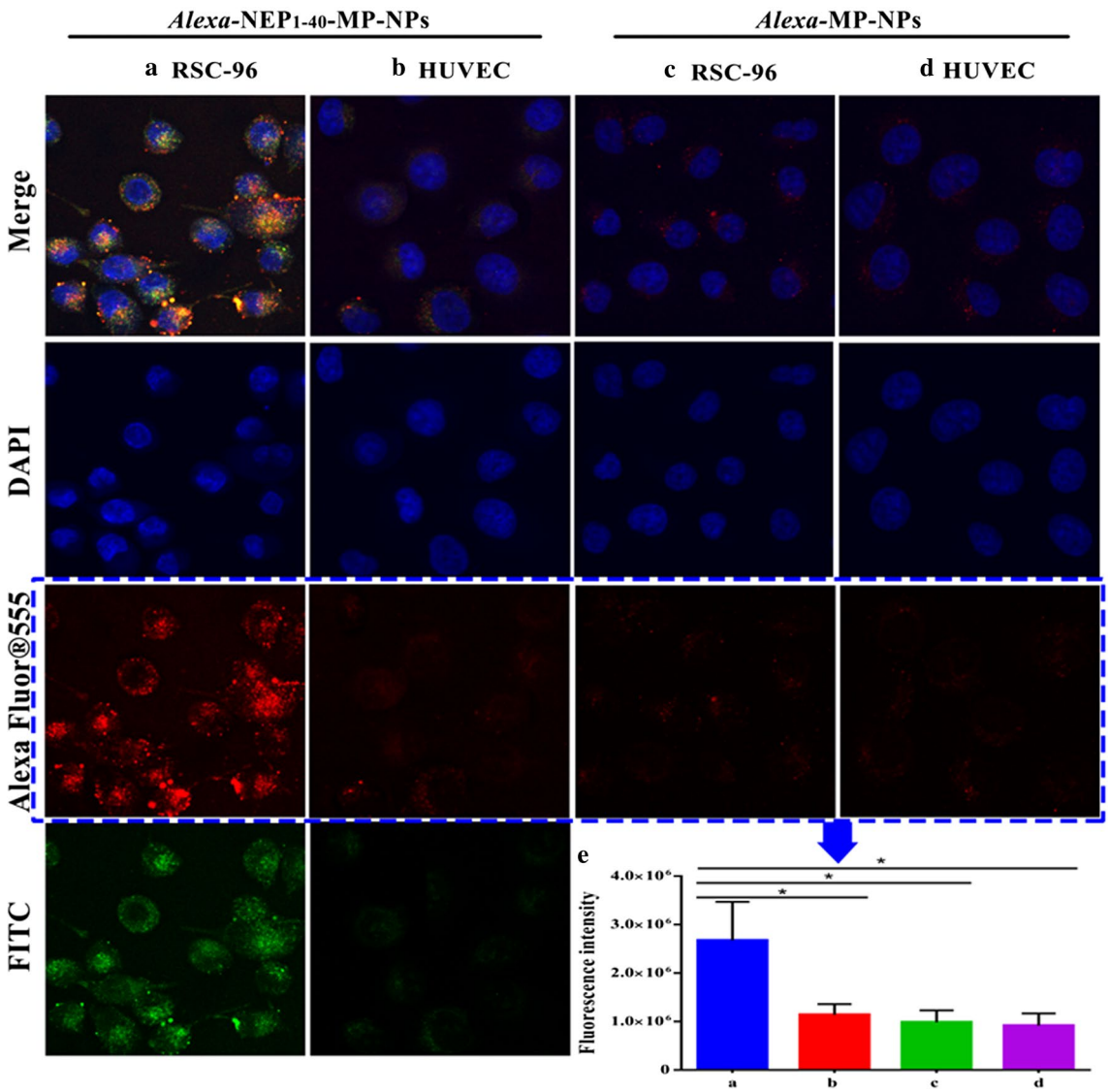

Fig. 4 Cellular uptake of NPs by RSC-96 cells and HUVECs. Fluorescently labeled NEP_{1-40} appeared green; fluorescently labeled NPs, red. Representative images showing **a** RSC-96 cells or **b** HUVECs treated with NEP_{1-40}-MP-NPs. Representative images showing **c** RSC-96 cells or **d** HUVECs treated with MP-NPs. **e** Summary of red fluorescence intensity analyzed by NIH Image-Pro Plus 6.0. Results are mean ± SD (n = 3)

blood biocompatibility and may be safe for clinical application.

Cellular uptake of NEP_{1-40}-MP-NPs

Uptake of free NEP_{1-40} and NEP_{1-40}-MP-NPs by Nogo-positive RSC-96 cells was analyzed. As a negative control, we performed the same experiments in Nogo-negative human umbilical vein endothelial cells (HUVECs). In these studies, NEP_{1-40} was labeled with FITC that could be detected in the green channel, while MP-NPs were labeled with Alexa Fluor® 555 that could be detected in the green channel. Co-localized red and green puncta were observed in cells treated with NEP_{1-40}-MP-NPs, suggesting that the peptide had successfully conjugated with MP-NPs (Fig. 4a). These intracellular fluorescent signals were much stronger in RSC-96 cells than in HUVECs (Fig. 4b). No fluorescence signal was detected from RSC-96 or HUVECs treated with MP-NPs (Fig. 4c, d). These results were confirmed in quantitative analysis (Fig. 4e). These results suggest that NEP_{1-40} significantly enhances NP uptake specifically in Nogo-positive cells.

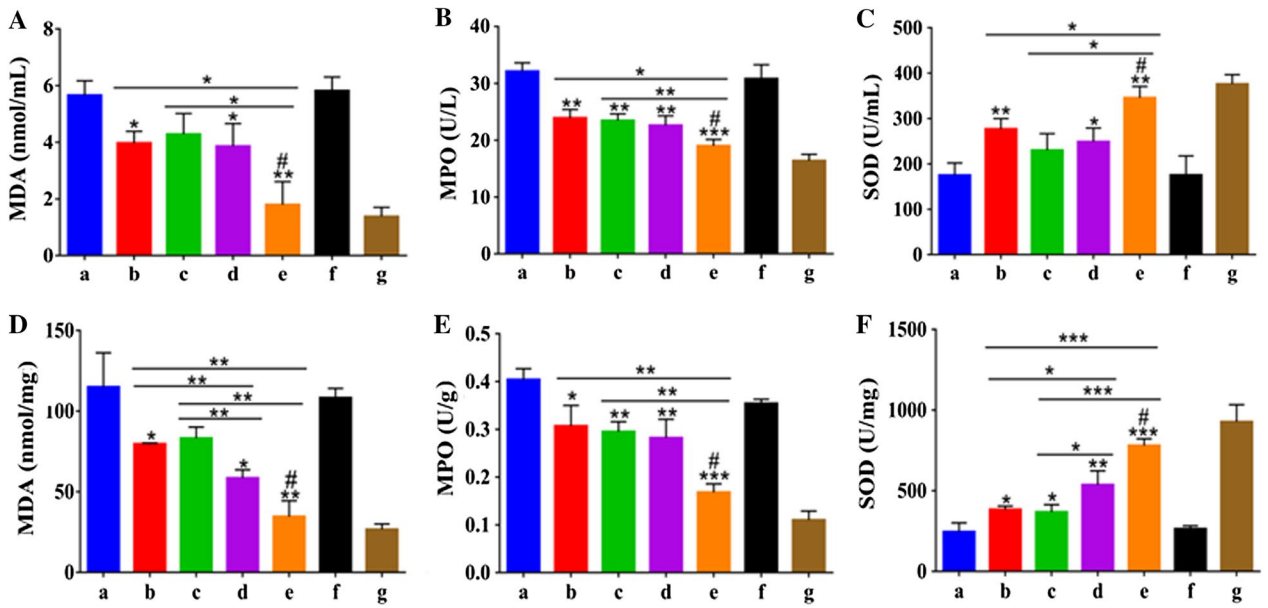

Fig. 5 Malondialdehyde (MDA), myeloperoxidase (MPO) and superoxide dismutase (SOD) levels in serum and spinal cord tissue after SCI in rats. **A** MDA in serum. **B** MPO in serum. **C** SOD in serum. **D** MDA in spinal cord. **E** MPO in spinal cord. **F** SOD in spinal cord. Animals were treated with (a) saline, (b) control MPS, (c) MP, (d) MP-NPs, (e) $NEP_{1\text{-}40}$-MP-NPs, (f) blank NPs, or (g) sham-operated. *P < 0.05, **P < 0.01, and ***P < 0.001 vs. saline; #P < 0.05 vs. MP-NPs. Data are mean ± SD (n ≥ 3)

Therapeutic efficacy of $NEP_{1\text{-}40}$-MP-NPs against SCI in a rat model of SCI

Levels of malondialdehyde (MDA) are an important indicator of lipid peroxidation by free radicals. MDA levels in serum and spinal cord were significantly lower in SCI rats treated with MPS, MP-NPs or $NEP_{1\text{-}40}$-MP-NPs than in saline-treated controls (Fig. 5A, D), in which methylprednisolone sodium succinate (MPS) was taking as the positive control. Levels in the $NEP_{1\text{-}40}$-MP-NP group were significantly lower than in the other treatment groups. These results indicate that MPS and MP encapsulated in NPs can alleviate free radical damage in rats after SCI, with $NEP_{1\text{-}40}$-MP-NPs showing the greatest effect.

Levels of myeloperoxidase (MPO) are an indicator of polymorphonuclear leukocyte accumulation and therefore of inflammation severity. Levels of MPO were significantly lower in animals treated with $NEP_{1\text{-}40}$-MP-NPs than in other treatment groups (Fig. 5B, E). These results indicate that free MP and MP encapsulated in NPs can alleviate the inflammatory response after SCI, with $NEP_{1\text{-}40}$-MP-NPs showing the greatest effect.

Superoxide dismutase (SOD) is a key enzyme in cellular antioxidant systems. SOD levels in serum and spinal cord tissue were significantly higher in animals treated with free MP, MPS, MP-NPs or $NEP_{1\text{-}40}$-MP-NPs than in saline-treated controls (Fig. 5C, F). Levels in the $NEP_{1\text{-}40}$-MP-NP group were significantly higher than in the other treatment groups. These results suggested that MP, MPS, MP-NPs or $NEP_{1\text{-}40}$-MP-NPs enhanced antioxidant capacity after spinal cord injury, with $NEP_{1\text{-}40}$-MP-NPs showing the strongest improvement.

Histopathology of spinal cord tissue at 1 day after the various treatments indicated that in animals treated with saline or blank NPs, neuronal nuclei and cell bodies were shrunken, synapses were reduced and ruptured, and hollow-like cell necrosis was observed (Fig. 6). Neurons were edematous and fewer in number, and they showed morphological changes. A large area of hemorrhage was observed in gray and white matter. Tissue from animals treated with MP, MPS, MP-NPs or $NEP_{1\text{-}40}$-MP-NPs showed more numerous neuronal cells and smaller hemorrhage area, with $NEP_{1\text{-}40}$-MP-NPs giving the best results.

Histopathology at 3 days after the various treatments showed necrosis of neuronal cells, exudation of inflammatory cells and proliferation of macrophages in the central area of the injury and in adjacent gray and white matter in animals treated with saline or blank NPs (Fig. 7). The number of inflammatory cells was reduced in animals treated with $NEP_{1\text{-}40}$-MP-NPs, MP, MPS or MP-NPs. $NEP_{1\text{-}40}$-MP-NP treatment was associated with the smallest number of inflammatory cells and greatest numbers of neuronal and glial cells.

Histopathology at 7 days after the various treatments showed vessel reconstruction in the central area of the

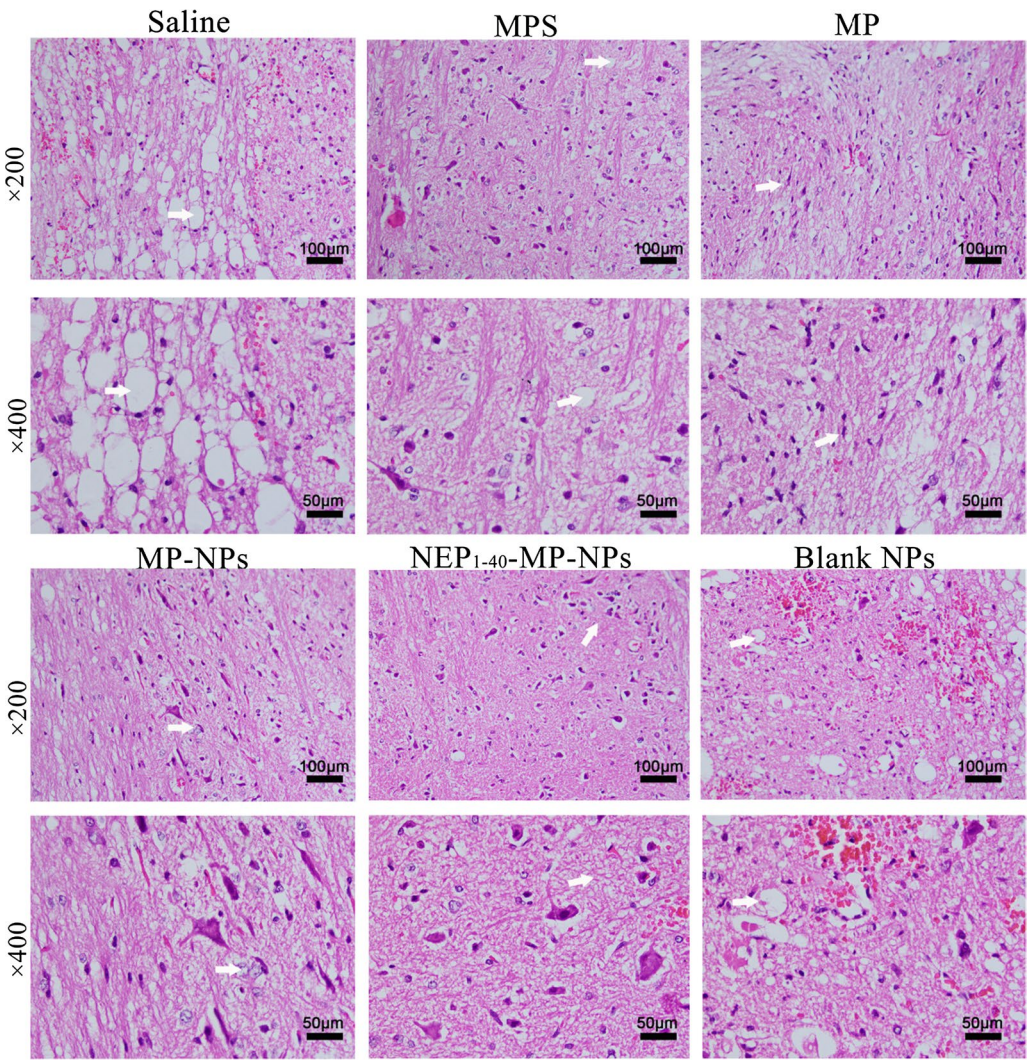

Fig. 6 Representative images showing histopathological analysis in spinal cord tissue after spinal cord injury at 1 day after intrathecal injection of saline, MPS (control), MP, MP-NPs, NEP_{1-40}-MP-NPs, or blank NPs (n = 3). Bold arrows indicate the location of lesions

lesion and adjacent sites, with scattered hemorrhage areas in animals treated with saline or blank NPs (Fig. 8). Hyperplasia of macrophages, necrosis of peripheral nerve cells, appearance of autophagosomes and foam cells were also observed. Treatment with NEP_{1-40}-MP-NPs, MP, MPS or MP-NPs showed improved proliferation of astrocytes and fibroblasts as well as reduced numbers of foam cells. Tissue from animals treated with NEP_{1-40}-MP-NPs group showed the greatest proliferation of glial cells and glial junction formation as well as smallest number of autophagosomes and least extensive scar formation. These results suggest that NEP_{1-40}-MP-NPs were the most effective at shortening the repair period after SCI.

Next we analyzed effects of the various treatments on trabecular bone microstructure using micro-computed tomography because SCI can induce osteoporosis [45, 46]. All treatment groups showed lower bone mineral density and bone thickness than in the sham group (Fig. 9A). Meanwhile, compared with the sham group, all the other treatment groups showed decreased number of bone trabeculae and the bones showed fractures and disruptions in the marrow cavity. Several bone microstructure parameters were significantly different between saline- and sham-treated animals as a result of SCI (Fig. 9B–G). While all parameters were similar between MP and MPS groups, many parameters differed between these groups and the NEP_{1-40}-MP-NP group. These results suggest that NEP_{1-40}-MP-NPs can promote restoration of bone microarchitecture after SCI.

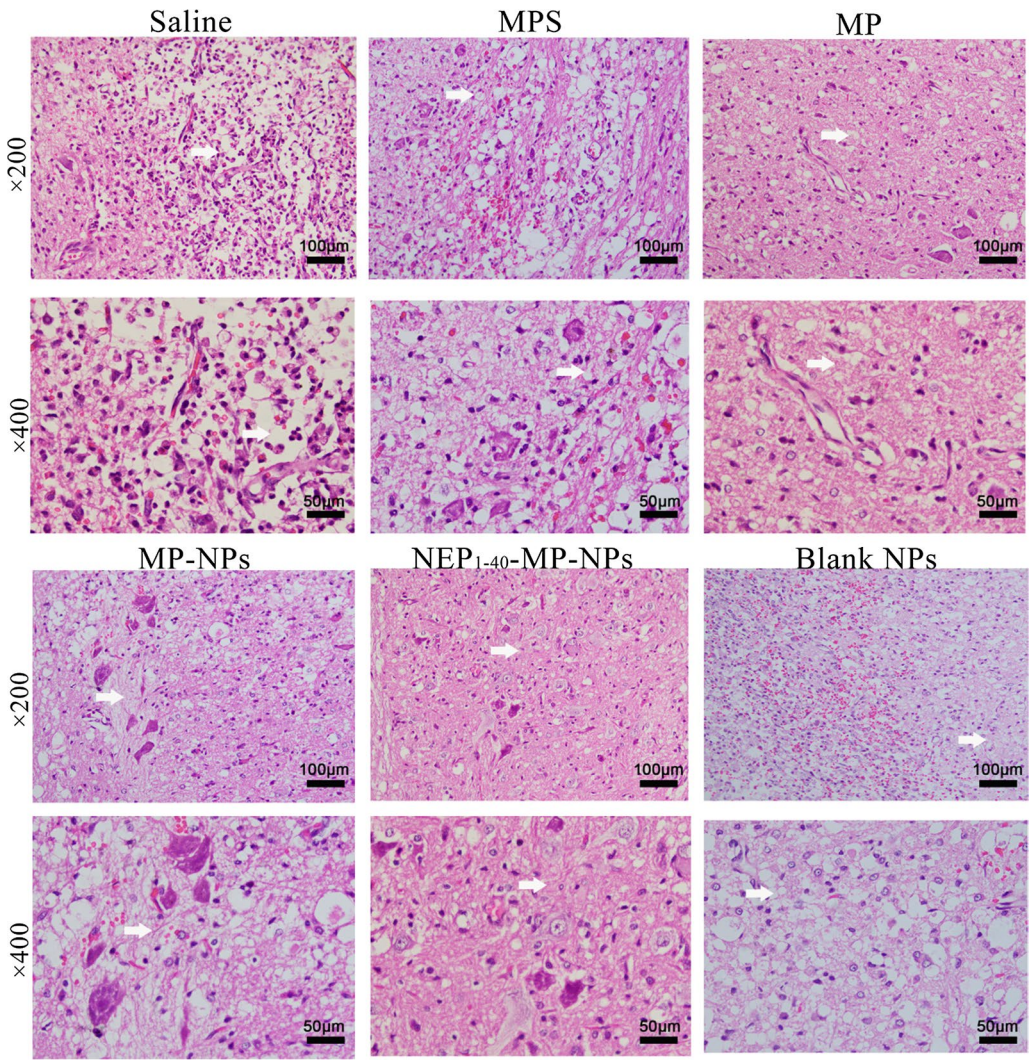

Fig. 7 Representative images showing histopathological analysis in spinal cord tissue after spinal cord injury at 3 days after intrathecal injection of saline, MPS (control), MP, MP-NPs, $NEP_{1\text{-}40}$-MP-NPs, or blank NPs (n = 3). Bold arrows indicate the location of lesions

Finally, we assessed the effects of the various treatments on hind limb neuromotor function in SCI rats (Fig. 10). Basso-Beattie-Bresnahan locomotor scores peaked on day 21 in the sham group (data not shown). At 1 day after SCI, scores were similar among all groups, but from day 14 onwards, scores increased gradually in the $NEP_{1\text{-}40}$-MP-NP and MP-NP groups. Scores on day 28 were 8 ± 1.461 in rats treated with $NEP_{1\text{-}40}$-MP-NPs and 7 ± 0.745 in animals treated with MP-NPs, significantly better than in other treatment groups ($P < 0.05$). Scores were significantly higher in the $NEP_{1\text{-}40}$-MP-NP group than in the MP-NP group.

Discussion

In the present study, we developed a novel $NEP_{1\text{-}40}$-MP-NP drug delivery system for enhancing the therapeutic effects of MP against SCI while allowing the use of lower doses, leading to lower side effects. Our MP-NPs were uniform and spherical and showed high encapsulation efficiency. Release of MP in vitro from $NEP_{1\text{-}40}$-MP-NPs was sustained and significantly slower than the release of free MP. These results agree with a previous report that NPs can serve as a drug reservoir, releasing the compounds in sustained manner [23–25]. $NEP_{1\text{-}40}$-MP-NPs were more effective than MP-NPs at reducing secondary spinal cord damage and loss of bone mineral density in a rat model of SCI, and the decorated NPs accelerated the repair process. We speculate that the

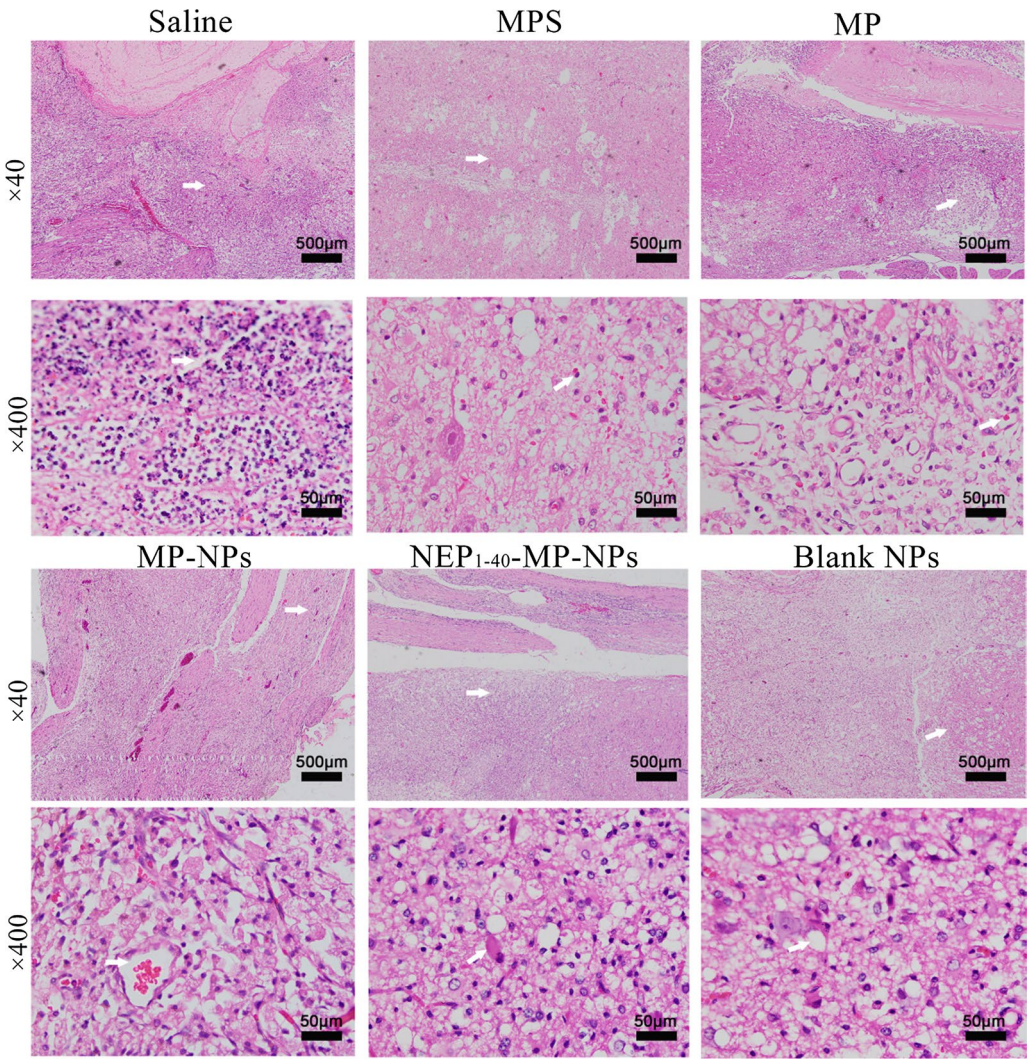

Fig. 8 Representative images showing histopathological analysis in spinal cord tissue after spinal cord injury at 7 days after intrathecal injection of saline, MPS (control), MP, MP-NPs, $NEP_{1\text{-}40}$-MP-NPs, or blank NPs (n = 3). Bold arrows indicate the location of lesions

ability of $NEP_{1\text{-}40}$-MP-NPs to enhance treatment effects of MP against SCI is because of the drug's slow release and $NEP_{1\text{-}40}$-mediated targeting of oligodendrocytes.

MP-NPs were prepared using blank HSA nanoparticles as the substructure of the core matrix. Critical to proper NP assembly was the manner in which materials were added, as well as the ratio of ethanol to water when disulfide bonds were formed in stabilized HSA-NPs. Glutathione was used as an effective reducing agent to break intra-molecular disulfide bonds in HSA, and it was maintained in the acid form by keeping pH low [26] through addition of HCl to the HSA solution and through dropwise addition to ethanol to reform inter-molecular disulfide bonds. These steps led to the formation of blank NPs, whose diameter was strongly affected by the ionic strength of the solution [33]. These blank NPs were exposed to air for at least 3 h with continuous stirring to enhance intermolecular disulfide bonds and glutathione oxidation; otherwise, nanoparticles quickly swelled up after adding water. These blank HSA-NPs were lyophilized in the presence of mannitol as a lyoprotectant. To this powder was added an MP-PEG compound that was prepared by mixing PEG_{400} and MP in ethanol, and then removing the ethanol. We hypothesize that MP-PEG formed through hydrogen bond formation as ethanol evaporated, since PEG_{400} has abundant hydrogen bond donors and acceptors. MP-NPs were prepared by adding MP-PEG liquid compound drop-wise to lyophilized blank HSA nanoparticles powder with stirring. The mixture was dispersed

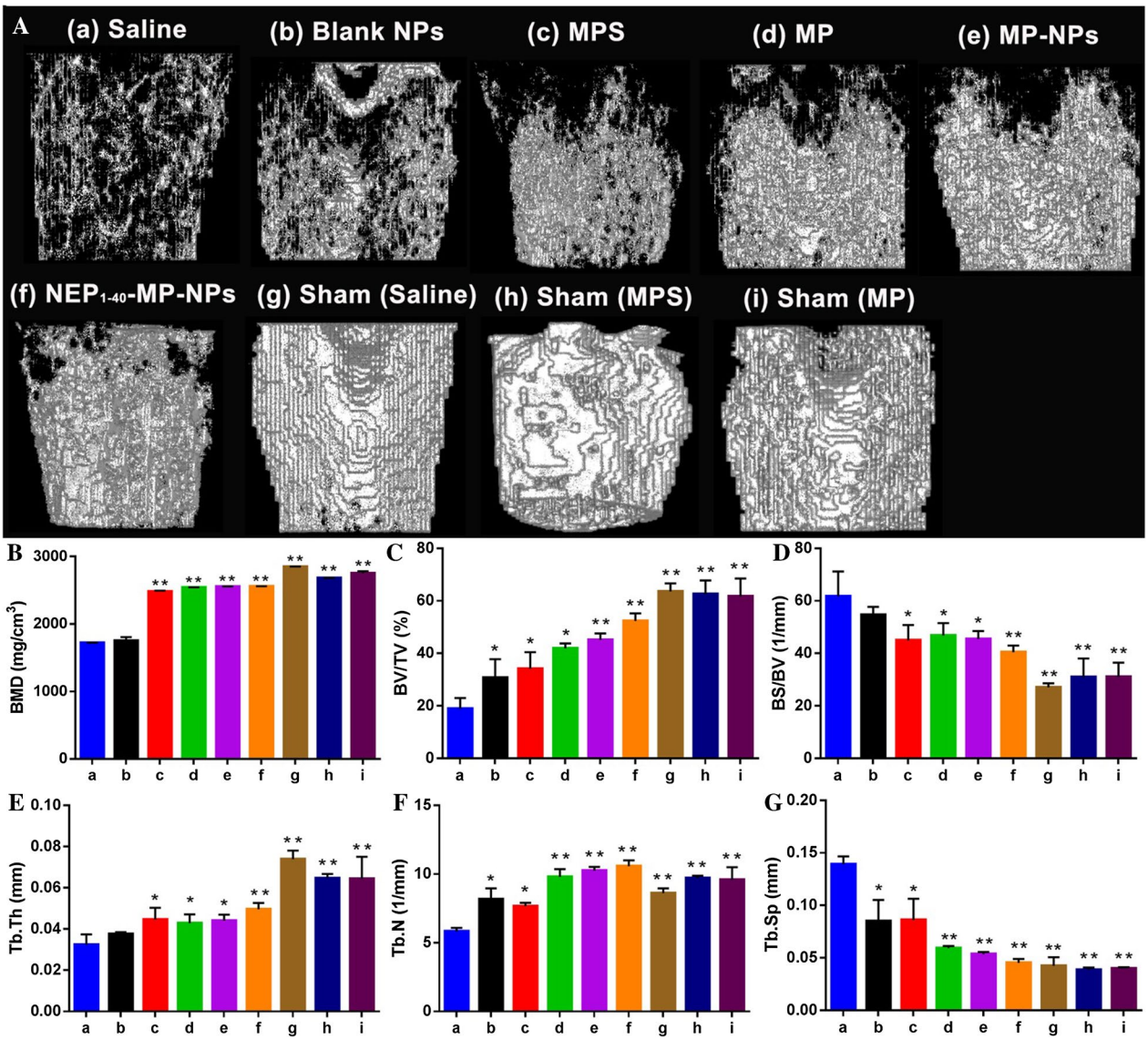

Fig. 9 Effects of the different formulations on trabecular bone microarchitecture in rats after spinal cord injury. **A** Representative micro-computed tomographs after treatment with (a) saline, (b) blank NPs, (c) control MPS, (d) MP, (e) MP-NPs, (f) NEP_{1-40}-MP-NPs, (g) saline sham, (h) MPS sham and (i) MP sham. **B** Bone mineral density (BMD). **C** Bone volume/total volume (BV/TV). **D** Bone surface area/bone volume (BS/BV). **E** Trabecular thickness (Tb.Th). **F** Trabecular number (Tb.N). **G** Trabecular spacing (Tb.Sp). *P < 0.05 or **P < 0.01 vs. saline. Data are mean ± SD (n = 3)

into acidified water. Due to the strong water polarity, hydrogen bonds between PEG and MP were broken, and the PEG formed new hydrogen bonds with the water. Because of the fluidity of MP-PEG and the affinity of HSA-NPs for hydrophobic drugs, MP readily entered the matrix structure of HSA-NPs. Since particle size is the main factor for ensuring homogeneous distribution of colloidal drug carrier systems [33], we subjected the mixture to intermittent ultrasound in a cold-water bath, forming milky white MP-NP solution. This desolvation technique is relatively simple and may allow better control of NEP_{1-40}-MP-NP size than emulsification or supercritical anti-solvent processes involving albumin coating.

Our assays with MDA and SOD suggest that NEP_{1-40}-MP-NPs can help scavenge free radicals. This may be analogous to the way in which nanoparticles based on cerium oxide, carbon, manganese, or platinum can scavenge reactive oxygen species [34]. Further work should assess the potential mechanism(s) of this activity by NEP_{1-40}-MP-NPs in greater detail.

NEP_{1-40}-MP-NPs showed good blood biocompatibility (Additional file 1: Figure S2) and therefore may be safe for clinical application, based on the ASTM E2524-08

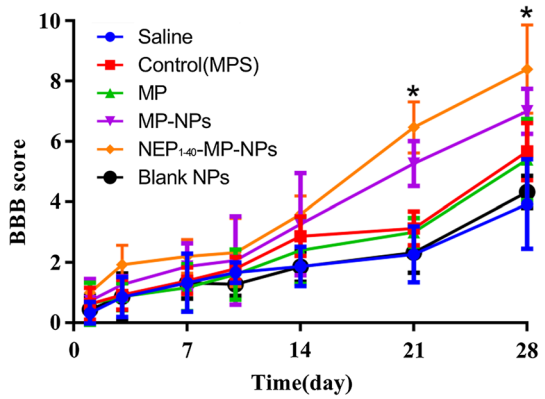

Fig. 10 Hind limb neuromotor function in rats after spinal cord injury as determined by the Basso–Beattie–Bresnahan locomotor score. Data are mean ± SD (n = 3). *P < 0.05 vs. MP-NPs

standard. Nevertheless, MP-NPs and NEP_{1-40}-MP-NPs showed some hemolytic effects. We speculate that this risk increases with higher NP concentration, since the probability of contacts between NPs and red blood cells increases.

This NEP_{1-40}-MP-NP drug delivery system may provide a new strategy for using MP against SCI. It may also provide a new platform for delivering other insoluble drugs to the CNS and other tissues, depending on the specificity coating applied.

Methods

Materials

NEP_{1-40} was synthesized by Top-peptide (Shanghai, China). NHS-PEG_{5000}-MAL was from Xi'an RuiXi (Xi'an, China). Ethanol, Tween-80 and PEG_{400} were obtained from Chengdu Kelon Chemical Reagent Factory (Chengdu, China). Human serum albumin, L-glutathione (98%), MP and 4′,6-diamidino-2-phenylindole (DAPI) were provided by Solarbio (Beijing, China). Dulbecco's modified Eagle's medium (DMEM) was obtained from Hammer Flew (Beijing, China). Fetal bovine serum was purchased from TianHang (Huzhou, China). Trypsin and Alexa Fluor® 555 were provided by Thermo Fisher Scientific (Waltham, MA, USA). Paraformaldehyde was obtained from Jinshan Chemical Company (Chengdu, China). MPO, SOD and MDA kits were purchased from the Nanjing Jiancheng Bioengineering Institute (Jiangshu, China).

Cells and animals

Rat Schwann cell line RSC-96 [35] and HUVECs were cultured in DMEM with fetal bovine serum (10%, v/v), penicillin (100 U/mL), and streptomycin (100 μg/mL). Cells were cultured at 37 °C in 5% CO_2.

Eight- to ten-week-old female Sprague–Dawley rats (150–220 g) were purchased from the Laboratory Animal Center of Southwest Medical University (Luzhou, China) and kept in controlled humidity, temperature, and lighting conditions. All animal experiments were approved by the Animal Ethics Committee of Southwest Medical University (permit 2016101101), and all animal operations were performed according to the guidelines of the Local Animal Use and Care Committee of Luzhou (Sichuan, China) and in accordance with the National Animal Welfare Law of China.

Preparation of NEP_{1-40}-MP-NPs

Blank NPs were prepared by desolvation [36, 37]. Briefly, glutathione powder (12 mg) was dissolved and mixed with 6 mL of HSA solution (5 mg/mL). The mixture was stirred slowly for 2 h at room temperature and adjusted to pH 3.45 using HCl solution (0.1 mol/L). The protein solution was then added to ethanol at 1 mL/min to form new intermolecular HSA disulfide bonds until the ethanol/water ratio was 3.5:1 (v/v). Then the solution was exposed to oxygen with stirring for at least 3 h to stabilize the newly formed disulfide bonds [32]. Finally, the suspension was diluted with 10 mL of distilled water, and the ethanol was removed under vacuum in a rotary evaporator at 37 °C. Excess glutathione was removed from the resulting suspension of blank nanoparticles by dialysis (mol. wt cut-off, 3500 Da) for 3 times (8 h each time). The suspension was then lyophilized with mannitol (5%) as lyoprotectant to obtain a powder of blank NPs.

To prepare the MP-PEG complex, 6 mg of MP and 100 μL of PEG_{400} were added into 4 mL of ethanol. Ethanol was removed under vacuum through rotary evaporation at 45 °C. MP-loaded NPs (MP-NPs) were prepared by ultrasonication. Briefly, 15 μL of the preformed MP-PEG complex was mixed with 15 mg of the blank NP powder and mixed with a small spatula. The mixture was dispersed into 5 mL of ultra-pure water. The dispersion was ultrasonicated intermittently at 90 W for 5 min using a probe ultrasonicator in a cold-water bath.

We prepared the peptide NEP_{1-40}-modified MP-NPs (NEP_{1-40}-MP-NPs) through sulfhydryl groups of NPs [35–38]. Briefly, to activate MP-NPs, the heterobifunctional cross linker of NHS-PEG_{5000}-MAL (16 mg) was dissolved in 1 mL of phosphate buffer (pH 8.0) and mixed with nanoparticle suspension (100 mg) at a molar ratio of 2:1 based on previous work [39]. The mixture was incubated with shaking (550 rpm) for 1 h at room temperature. Then the activated MP-NPs were purified by two cycles of ultra-centrifugation at 15,000*g* for 8 min to remove un-reacted NHS-PEG_{5000}-MAL. The pellet was then re-dispersed in 1 mL of phosphate buffer (pH 8.0)

and incubated with $NEP_{1\text{-}40}$ peptide (870 μg) at a molar ratio of 1:1 for 1 h with stirring (600 rpm); this molar ratio was based on a previous report that the terminal cysteine (Cys) of $NEP_{1\text{-}40}$ reacts with maleimide in a molar ratio of 1:1 [39]. To remove excess small molecules, the reaction solution was centrifuged for 10 min at 6000*g* through an ultrafiltration centrifuge tube with molecular weight cutoff at 30 kDa. The ultrafiltration was repeated four times to obtain purified $NEP_{1\text{-}40}$-MP-NPs.

Alexa-HSA was conjugated as described previously [39]. Briefly, 1 mg of the succinimidyl ester fluorophore Alexa Fluor® 555 and 2 mL of HSA (20%) were dissolved in bicarbonate buffer (0.05 M, pH 8.3) and stirred in the dark for 2 h at room temperature. The solution was then purified by dialysis in ultrapure water for 48 h to obtain Alexa-HSA. Alexa-labeled MP-NPs or $NEP_{1\text{-}40}$-MP-NPs (Alexa-MP-NPs, Alexa-$NEP_{1\text{-}40}$-MP-NPs) were obtained by adding a small amount (5%) of Alexa-HSA to the components at the beginning of preparing MP-NPs or $NEP_{1\text{-}40}$-MP-NPs, respectively.

Characterization of NPs

The average particle size and zeta potential of blank NPs, MP-NPs, and $NEP_{1\text{-}40}$-MP-NPs were measured in ultrapure water at 25 °C using dynamic light scattering (Malvern Zetasizer Nano ZS, Malvern, UK). NPs were stained with uranyl acetate and examined using transmission electron microscopy (JEM-1200EX, Japan).

Fourier-transform infrared spectroscopy (IRAffinity-1S, Shimadzu, Japan) was used to analyze MP-PEG and $NEP_{1\text{-}40}$-MP-NPs. Samples were blended with KBr at a ratio of 1:100 (w/w). KBr discs were produced under hydraulic pressure of 10,000 psi. Spectra were recorded from KBr pellets at a resolution of 4 mm/s over the wavenumber range 500–4000 cm^{-1}. Experiments were performed three times for each sample. MP, PEG, and a physical mixture of MP and PEG were analyzed in parallel as controls for analysis of the MP-PEG complex. MP, blank NPs, NHS-PEG5000-MAL, $NEP_{1\text{-}40}$, and the physical mixture of these four components were analyzed in parallel as controls for analysis of $NEP_{1\text{-}40}$-MP-NPs.

The conjugation rate during formation of $NEP_{1\text{-}40}$-MP-NPs was analyzed based on fluorescently labeled $NEP_{1\text{-}40}$. Ultrafiltration was used to remove un-reacted $NEP_{1\text{-}40}$, so the fluorescence of $NEP_{1\text{-}40}$ was measured in the filtrate and retained sample in triplicate at an excitation wavelength of 488 nm and emission wavelength of 517 nm using an F-7000 fluorescence spectrophotometer (Hitachi, Tokyo, Japan). It was carried out in in triplicate. The conjugation rate was calculated by determining the total fluorescence of the filtrates (W_{free}) and subtracting it from the total fluorescence before ultrafiltrations (W_{total}): conjugation rate (%) = $(W_{total} - W_{free})/W_{total} \times 100\%$.

To complement this fluorescence approach, we also determined the conjugation rate using HPLC. Measurements were run at 25 °C on a ZORBAX Eclipse XDB-C18 column (5 μm, 250 × 4.6 mm) with gradient elution in a mobile phase of acetonitrile (A) and water (B) in 0.05% trifluoroacetic acid at a flow rate of 1.0 mL/min. The linear gradient (A:B) ran from 5:95 at 0 min to 95:5 at 20 min. The detection wavelength was 214 nm. The conjugation rate (%) was calculated as $(W_{total} - W_{free})/W_{total} \times 100\%$, where W_{total} refers to the $NEP_{1\text{-}40}$ content in the initial solution and W_{free} refers to the $NEP_{1\text{-}40}$ content in the collected filtrate.

MP encapsulation and release in vitro

Encapsulation efficiency and drug loading rate of MP-NPs were estimated by ultrafiltration. A predetermined volume of MP-NPs was added to an ultrafiltration tube with a 30-kDa molecular weight cut-off, and free MP in the filtrate (W_{free}) was determined by HPLC (Agilent 1260 Infinity, USA) with a photodiode array detector. Measurements were performed at 25 °C on a C18 column (5 μm, 250 × 4.6 mm, Kromasil). The mobile phase consisted of acetonitrile and ultrapure water (32:68, v/v) and the detector was set at a wavelength of 254 nm.

The same amount of NP suspension was added to cold acetonitrile and vortexed for 5 min to extract MP. The extract was concentrated by centrifugation at 9500*g* for 5 min at 25 °C. The supernatant was assayed by HPLC to quantify the total MP in the nanoparticle system (W_{total}). The total weight of the same amount of dried nanoparticles (W_{NPs}) was also measured. The encapsulation efficiency and drug-loading rate were calculated using the following formulas:

$$\text{Encapsulation efficiency (\%)} = (W_{total} - W_{free})/W_{total} \times 100\%$$

$$\text{Drug loading rate (\%)} = (W_{total} - W_{free})/W_{NPs} \times 100\%.$$

Drug release in vitro was analyzed in phosphate-buffered saline (PBS, pH 7.4) containing 0.3% Tween-80 [40]. Three batches of freshly prepared $NEP_{1\text{-}40}$-MP-NPs and free MP were put into separate dialysis bags (mol. wt cut-off, 3500 Da) and suspended in 30 mL of release medium. The sealed vials were put in a water bath at 37 °C with slow stirring. At 0.5, 1, 2, 4, 6, 8, 12, 24, 36, 48, 72, 96, and 120 h, sample (1.0 mL) was removed and replaced with the same amount of fresh medium. The sample was fixed with 2 mL methanol and filtered through a 0.22-μm membrane (Millipore). MP content in all samples was determined by HPLC as described above.

Cellular uptake of NEP_{1-40}-MP-NPs

In order to track intracellular transport of nanoparticles, we prepared Alexa-NEP_{1-40}-MP-NPs and, as a negative control, Alexa-MP-NPs. Alexa-NEP_{1-40}-MP-NPs emit fluorescence in the red and green channels [40], while Alexa-MP-NPs emit only in the red channel due to the lack of FITC-labeled NEP_{1-40}. Experiments were conducted in Nogo-positive RSC-96 cells, with Nogo-negative HUVECs as controls. RSC-96 cells and HUVECs were plated at 5×10^4 cells/well on sterile coverslips in 24-well plates 1 day before the cellular uptake assay. Cultures at ~70–80% confluence were washed three times with PBS and then incubated with 1 mL of the same concentrations of Alexa-NEP_{1-40}-MP-NPs or Alexa-MP-NPs for 4 h at 37 °C. Cells were rinsed with PBS three times and fixed with paraformaldehyde (4%) for 15 min [41], then stained with 150 μL of DAPI (5 mg/mL) for 8 min. Subsequently, coverslips were sealed with glycerol and observed under a confocal laser scanning microscope, in which the emission of Alexa flour and FITC was set at 580 nm and 519 nm, respectively. Cellular uptake was quantified using NIH Image-Pro Plus 6.0.

Effects of NEP_{1-40}-MP-NPs in a rat model of SCI

A rat model of SCI was established using a modified Allen's weight drop method [42]. Briefly, Sprague–Dawley rats were anaesthetized with an intraperitoneal injection of chloral hydrate (350 mg/kg). The hair on the back of the rat was removed and the skin was disinfected with iodine at the incision site. A dorsal longitudinal midline incision (3 cm) was made over the T9–T11 vertebral region using sterile tools. Fascia and para vertebral muscles were gently dissected to expose the lamina and transverse process. Spinal cord contusion was made by dropping a 15-g rod from a height of 10 cm to directly hit the exposed dorsal side of the spinal cord. The rod was removed immediately after the injury. For the sham group, the T10 lamina was opened and the spinal cord was exposed, but not subjected to spinal cord contusion. The animals were randomly divided into the following nine groups (n = 7/group): (a) SCI (saline), (b) SCI (blank NPs), (c) SCI (MPS), (d) SCI (MP), (e) SCI (MP-NPs), (f) SCI (NEP_{1-40}-MP-NPs), (g) Sham (Saline), (h) Sham (MPS) and (i) Sham (MP). Each group received a single intrathecal injection (100 μL) of the corresponding treatment. After intrathecal injection, the incision was closed using 4-0 sutures. Cefazolin (100 mg/kg) was administered by intramuscular injection once a day for 7 days to prevent infection. Rats were kept in warm-water pads until waking up from anesthesia. Manual bladder oppression was performed twice a day until the rats were able to urinate spontaneously.

At 1 day after SCI, serum and spinal cord tissue from each group (n = 3) were collected for the detection of MDA, MPO, and SOD [43–45]. All assays were performed according to the instructions in the ELISA kits. For histological examination, spinal cord tissue samples were collected on days 1, 3, and 7 after SCI and fixed in neutral-buffered formalin (10%), dehydrated through a graded series of ethanol solutions and embedded in paraffin. Paraffin sections (5 μm) were prepared and stained with hematoxylin and eosin.

To assess trabecular bone microstructure in rats treated with NEP_{1-40}-MP-NPs, animals were sacrificed on day 14 after SCI. The left femur was carefully separated from the surrounding soft tissue and fixed in formalin at room temperature for 24 h. The skeletal microarchitecture (n = 3) was analyzed using high-resolution micro-computed tomography (SIEMENS Healthcare, Berlin and Munich, Germany). Measurement parameters were voltage, 80 kV; current, 80 μA; exposure time, 2.96 s; total rotation angle, 360°; and rotation increment angle, 0.5; scanning resolution, 14 μm/slice. Femur specimens were placed in a 20-mm-diameter sample tube, perpendicular to the scanning axis with a total reconstructed height of 12 mm. One scan took approximately 30 min. Scans were transferred to a workstation for 3-D reconstruction. A cylindrical volume of interest with 3.0-mm diameter and 3.0-mm height was defined for analysis of bone mineral density (BMD), bone volume normalized to total volume (BV/TV), bone surface normalized to bone volume (BS/BV), trabecular thickness (Tb. Th), trabecular number (Tb. N), and trabecular separation (Tb. Sp).

The Basso–Beattie–Bresnahan locomotor rating scale (0–21 points) was used to evaluate the neuromotor function in all rats in a quiet environment at 1, 3, 7, 10, 14, 21 and 28 days after SCI. Two trained technicians blinded to experimental groups performed the assessments. Animals were exposed to an open field of a square plastic box ($100 \times 100 \times 5$ cm) for 4 min. Scores were assigned based on movement coordination of limb, paw placement and tail balance [46]. No obvious movement of the hind legs was counted as 0 points. Animals were scored with 21 points if they showed normal locomotion, continuous walking on the paws with a bent tail, normal motor co-ordination for the fore and hind limbs, trunk stability, floor gripping with the toes while moving forward, and alignment of the paws with body movement.

Statistical analysis

Results are expressed as mean ± standard deviation (SD) and analyzed using GraphPad Prism 6.0 (GraphPad Software, La Jolla, CA, USA). Statistical

comparisons between different groups were conducted by one-way analysis of variance (ANOVA). Differences between groups were considered statistically significant when $P < 0.05$.

Additional file

Additional file 1: Figure S1. Comparison of fluorescence intensity in (a) retained sample and (b) filtrate after sequential ultrafiltrations. Results are mean ± SD (n = 3). **Figure S2.** Hemolytic rates of different formulations. Results are mean ± SD (n = 3).

Abbreviations

BSA: bovine serum albumin; DMEM: Dulbecco's Modified Eagle medium; HSA: human serum albumin; MDA: malondialdehyde; MP: methylprednisolone; MP-NPs: methylprednisolone-loaded nanoparticles; MPO: myeloperoxidase; MPS: methylprednisolone sodium succinate; MTT: 3-(4,5-dimethylthiazol-2-yl)-2,5-diphenyltetrazolium bromide; NEP_{1-40}-MP-NPs: NEP_{1-40}-modified nanoparticles loaded with methylprednisolone; PBS: phosphate-buffered solution; PDI: polydispersity index; SOD: superoxide dismutase.

Authors' contributions

YL, CHL, JL, JH, QLZ and RLD performed experiments. YL, ZRZ, JL, JH and RLD analyzed data. YL, CHL, JL, ZRZ and RLD wrote the paper. YL, CHL, JL, and RLD designed the study. All authors read and approved the final manuscript.

Author details

[1] Department of Pharmaceutical Sciences, School of Pharmacy, Southwest Medical University, Luzhou 646000, China. [2] Luzhou TCM Hospital, Luzhou 646000, China. [3] Key Laboratory of Drug Targeting and Drug Delivery System, Ministry of Education (Sichuan University), Chengdu 610000, China. [4] Key Laboratory of Medical Electrophysiology, Ministry of Education, Institute of Cardiovascular Research of Southwest Medical University, Luzhou 646000, China.

Acknowledgements

The authors are grateful for support from the Key Laboratory of Medical Electrophysiology of the Ministry of Education, the Collaborative Innovation Center for Prevention and Treatment of Cardiovascular Disease, the Drug Discovery Research Center, the Department of Medicinal Chemistry, and the School of Pharmacy of Southwest Medical University (Luzhou, China).

Competing interests

The authors declare that they have no competing interest.

Availability of data and materials

All data generated and materials used in this study are included in the manuscript and corresponding additional files.

Consent for publication

All authors agreed to submit this manuscript.

Ethics approval and consent to participate

The experimental protocol was approved by the Institutional Ethics Committee and complied with the regulations of the Luzhou Council on Animal Use.

Funding

This work was supported by the General Program of Science and Technology Agency of the Sichuan Province (2017JY0160), the Collaborative Fund of Luzhou Government and Southwest Medical University (2016LZXNYD-J06, 2017LZXNYD-T07), Key Fund and the Youth Fund and the Transformation Project of Science and Technology Achievements of Southwest Medical University (2018-ZRZD-018, 2017-ZRQN-073, 2018002), the Science and Technology Project of the Health Planning Committee of Sichuan (18PJ547), the Opening Project of the Key Laboratory of Drug Targeting and Drug Delivery System of the Ministry of Education (Sichuan University), Key Science and Technology Project of Luzhou Government (2018-SYF-19, 2018-RCM-66), the Collaborative Project of Luzhou TCM Hospital and Southwest Medical University (2017-LH004).

Publisher's Note

Received: 13 October 2018 Accepted: 9 January 2019
Published online: 22 January 2019

References

1. Chen C, Zhang YP, Sun Y, Xiong W, Shields LBE, Shields CB, Jin X, Xu XM. An in vivo duo-color method for imaging vascular dynamics following contusive spinal cord injury. J Vis Exp. 2017;130:1–10.
2. Cadotte DW, Fehlings MG. Spinal cord injury: a systematic review of current treatment options. Clin Orthop Relat Res. 2011;469:732–41.
3. Becker D, Sadowsky CL, McDonald JW. Restoring function after spinal cord injury. Neurologist. 2003;9:1–15.
4. Christopher D, Witiw MD, Michael G, Fehlings MD. Acute spinal cord injury. J Spinal Disord Tech. 2015;28:202–10.
5. Hyun JK, Kim HW. Clinical and experimental advances in regeneration of spinal cord injury. J Tissue Eng. 2010;2010:650857.
6. Gorio A, Madaschi L, Di Stefano B, Carelli S, Di Giulio AM, De Biasi S, Coleman T, Cerami A, Brines M. Methylprednisolone neutralizes the beneficial effects of erythropoietin in experimental spinal cord injury. Proc Natl Acad Sci USA. 2005;102:16379–84.
7. Chvatal SA, Kim YT, Bratt-Leal AM, Lee H, Bellamkonda RV. Spatial distribution and acute anti-inflammatory effects of Methylprednisolone after sustained local delivery to the contused spinal cord. Biomaterials. 2008;29:1967–75.
8. Druschel C, Schaser KD, Schwab JM. Current practice of methylprednisolone administration for acute spinal cord injury in Germany: a national survey. Spine. 2013;38:E669–77.
9. Chen HC, Fong TH, Lee AW, Chiu WT. Autophagy is activated in injured neurons and inhibited by methylprednisolone after experimental spinal cord injury. Spine. 2012;37:470–5.
10. Kwon BK, Fisher CG, Dvorak MF, Tetzlaff W. Strategies to promote neural repair and regeneration after spinal cord injury. Spine. 2005;30:S3–13.
11. Xu J, Fan G, Chen S, Wu Y, Xu XM, Hsu CY. Methylprednisolone inhibition of TNF-alpha expression and NF-kB activation after spinal cord injury in rats. Brain Res Mol Brain Res. 1998;59:135–42.
12. Sun YY, Wang CY, Hsu MF, Juan SH, Chang CY, Chou CM, Yang LY, Hung KS, Xu J, Lee YH, Hsu CY. Glucocorticoid protection of oligodendrocytes against excitotoxin involving hypoxia-inducible factor-1alpha in a cell-type-specific manner. J Neurosci. 2010;30:9621–30.
13. Lee JM, Yan P, Xiao Q, Chen S, Lee KY, Hsu CY, Xu J. Methylprednisolone protects oligodendrocytes but not neurons after spinal cord injury. J Neurosci. 2008;28:3141–9.
14. Karabey-Akyurek Y, Gurcay AG, Gurcan O, Turkoglu OF, Yabanoglu-Ciftci S, Eroglu H, Sargon MF, Bilensoy E, Oner L. Localized delivery of methylprednisolone sodium succinate with polymeric nanoparticles in experimental injured spinal cord model. Pharm Dev Technol. 2017;22:972–81.
15. Aguayo JMDT. Side effects of steroid use in patients with traumatic spinal cord injury. Coluna/Columna. 2015;14:45–9.
16. Chikuda H, Yasunaga H, Takeshita K, Horiguchi H, Kawaguchi H, Ohe K, Fushimi K, Tanaka S. Mortality and morbidity after high-dose methylprednisolone treatment in patients with acute cervical spinal cord injury: a propensity-matched analysis using a nationwide administrative database. Emerg Med J. 2014;31:201–6.
17. Cerqueira SR, Oliveira JM, Silva NA, Leite-Almeida H, Ribeiro-Samy S, Almeida A, Mano JF, Sousa N, Salgado AJ, Reis RL. Microglia response and in vivo therapeutic potential of methylprednisolone-loaded dendrimer nanoparticles in spinal cord injury. Small. 2013;9:738–49.
18. Qi L, Jiang H, Cui X, Liang G, Gao M, Huang Z, Xi Q. Synthesis of methylprednisolone loaded ibuprofen modified dextran based nanoparticles

and their application for drug delivery in acute spinal cord injury. Oncotarget. 2017;8(59):99666–80.
19. Shi Y, Kim S, Huff TB, Borgens RB, Park K, Shi R, Cheng JX. Effective repair of traumatically injured spinal cord by nanoscale block copolymer micelles. Nat Nanotechnol. 2010;5:80–7.
20. Kim YT, Caldwell JM, Bellamkonda RV. Nanoparticle-mediated local delivery of methylprednisolone after spinal cord injury. Biomaterials. 2009;30:2582–90.
21. Cho Y, Shi R, Borgens R, Ivanisevic A. Repairing the damaged spinal cord and brain with nanomedicine. Small. 2008;4:1676–81.
22. Yang Z, Gong W, Wang Z, Li B, Li M, Xie X, Zhang H, Yang Y, Li Z, Li Y, et al. A novel drug-polyethylene glycol liquid compound method to prepare 10-hydroxycamptothecin loaded human serum albumin nanoparticle. Int J Pharm. 2015;490:412–28.
23. Elzoghby AO, Samy WM, Elgindy NA. Albumin-based nanoparticles as potential controlled release drug delivery systems. J Control Release. 2012;157:168–82.
24. Watcharin W, Schmithals C, Pleli T, Koberle V, Korkusuz H, Huebner F, Zeuzem S, Korf HW, Vogl TJ, Rittmeyer C, et al. Biodegradable human serum albumin nanoparticles as contrast agents for the detection of hepatocellular carcinoma by magnetic resonance imaging. Eur J Pharm Biopharm. 2014;87:132–41.
25. Liu L, Bi Y, Zhou M, Chen X, He X, Zhang Y, Sun T, Ruan C, Chen Q, Wang H, Jiang C. Biomimetic human serum albumin nanoparticle for efficiently targeting therapy to metastatic breast cancers. ACS Appl Mater Interfaces. 2017;9:7424–35.
26. Weber C, Kreuter J, Langer K. Desolvation process and surface characteristics of HSA-nanoparticles. Int J Pharm. 2000;196:197–200.
27. Song Z, Lu Y, Zhang X, Wang H, Han J, Dong C. Novel curcumin-loaded human serum albumin nanoparticles surface functionalized with folate: characterization and in vitro/*vivo* evaluation. Drug Des Devel Ther. 2016;10:2643–9.
28. GrandPre T, Li S, Strittmatter SM. Nogo-66 receptor antagonist peptide promotes axonal regeneration. Nature. 2002;417:547–51.
29. GrandPre T, Nakamura F, Vartanian T, Strittmatter SM. Identification of the Nogo inhibitor of axon regeneration as a Reticulon protein. Nature. 2000;403:439–44.
30. Gou X, Wang Q, Yang Q, Xu L, Xiong L. TAT-NEP1-40 as a novel therapeutic candidate for axonal regeneration and functional recovery after stroke. J Drug Target. 2011;19:86–95.
31. Xu J, He J, He H, Peng R, Xi J. Comparison of RNAi NgR and NEP1-40 in acting on axonal regeneration after spinal cord injury in rat models. Mol Neurobiol. 2017;54:8321–31.
32. Langer K, Balthasar S, Vogel V, Dinauer N, von Briesen H, Schubert D. Optimization of the preparation process for human serum albumin (HSA) nanoparticles. Int J Pharm. 2003;257:169–80.
33. Ulbrich K, Knobloch T, Kreuter J. Targeting the insulin receptor: nanoparticles for drug delivery across the blood–brain barrier (BBB). J Drug Target. 2011;19:125–32.
34. Ferreira CA, Ni D, Rosenkrans ZT, Cai W. Scavenging of reactive oxygen and nitrogen species with nanomaterials. Nano Res. 2018;11:4955–84.
35. Eckharter C, Junker N, Winter L, Fischer I, Fogli B, Kistner S, Pfaller K, Zheng B, Wiche G, Klimaschewski L, Schweigreiter R. Schwann cell expressed Nogo-B modulates axonal branching of adult sensory neurons through the Nogo-B receptor NgBR. Front Cell Neurosci. 2015;9:454.
36. Jahanban EA, Dastmalchi S, Davaran SA. Simple improved desolvation method for the rapid preparation of albumin nanoparticles. Int J Biol Macromol. 2016;91:703–9.
37. Moghimi SM, Hunter AC, Murray JC. Long-circulating and target-specific nanoparticles: theory to practice. Pharmacol Rev. 2001;53:283–318.
38. Weber C, Coester C, Kreuter J, Langer K. Desolvation process and surface characterisation of protein nanoparticles. Int J Pharm. 2000;194:91–102.
39. Look J, Wilhelm N, von Briesen H, Noske N, Gunther C, Langer K, Gorjup E. Ligand-modified human serum albumin nanoparticles for enhanced gene delivery. Mol Pharm. 2015;12:3202–13.
40. Ulbrich K, Hekmatara T, Herbert E, Kreuter J. Transferrin- and transferrin-receptor-antibody-modified nanoparticles enable drug delivery across the blood–brain barrier (BBB). Eur J Pharm Biopharm. 2009;71:251–6.
41. Luo Y, Liu Z, Zhang X, Huang J, Yu X, Li J, Xiong D, Sun X, Zhong Z. Effect of a controlled-release drug delivery system made of oleanolic acid formulated into multivesicular liposomes on hepatocellular carcinoma in vitro and *in vivo*. Int J Nanomed. 2016;11:3111–29.
42. Zhang D, Ma G, Hou M, Zhang T, Chen L, Zhao C. The neuroprotective effect of puerarin in acute spinal cord injury rats. Cell Physiol Biochem. 2016;39:1152–64.
43. Zhao BL, Li WT, Zhou XH, Wu SQ, Cao HS, Bao ZR, An LB. Effective robotic assistive pattern of treadmill training for spinal cord injury in a rat model. Exp Ther Med. 2018;15:3283–94.
44. Fu D, Liu H, Li S, Chen L, Yao J. Antioxidative and antiapoptotic effects of delta-opioid peptide [D-Ala(2), D-Leu(5)] enkephalin on spinal cord ischemia–reperfusion injury in rabbits. Front Neurosci. 2017;11:603.
45. Yuan B, Pan S, Zhang WW. Effects of gangliosides on expressions of caspase-3 and NGF in rats with acute spinal cord injury. Eur Rev Med Pharmacol Sci. 2017;21:5843–9.
46. Barros Filho TE, Molina AE. Analysis of the sensitivity and reproducibility of the Basso, Beattie, Bresnahan (BBB) scale in Wistar rats. Clinics (Sao Paulo). 2008;63:103–8.